Naval Research Laboratory
Washington, DC 20375-5320

NRL/MR/5317--19-9915

Tutorial: Applying Phase-Mode Theory to the Design of Cylindrical Arrays

W. Mark Dorsey
Anna Stumme

Radar Analysis Branch
Radar Division

Jeffrey O. Coleman

KeyW Corporation Consultant
Hanover, MD

September 27, 2019

REPORT DOCUMENTATION PAGE

Form Approved
OMB No. 0704-0188

1. REPORT DATE *(DD-MM-YYYY)*
27-09-2019

2. REPORT TYPE
NRL Memorandum Report

3. DATES COVERED *(From - To)*

4. TITLE AND SUBTITLE
Tutorial: Applying Phase-Mode Theory to the Design of Cylindrical Arrays

5a. CONTRACT NUMBER

5b. GRANT NUMBER

5c. PROGRAM ELEMENT NUMBER

6. AUTHOR(S)
W. Mark Dorsey, Anna Stumme, and Jeffrey O. Coleman*

5d. PROJECT NUMBER

5e. TASK NUMBER

5f. WORK UNIT NUMBER

7. PERFORMING ORGANIZATION NAME(S) AND ADDRESS(ES)
Naval Research Laboratory
4555 Overlook Avenue, SW
Washington, DC 20375-5320

8. PERFORMING ORGANIZATION REPORT NUMBER
NRL/MR/5317--19-9915

9. SPONSORING / MONITORING AGENCY NAME(S) AND ADDRESS(ES)

10. SPONSOR / MONITOR'S ACRONYM(S)

11. SPONSOR / MONITOR'S REPORT NUMBER(S)

12. DISTRIBUTION / AVAILABILITY STATEMENT
DISTRIBUTION STATEMENT A: Approved for public release; distribution is unlimited.

13. SUPPLEMENTARY NOTES
*KeyW Corporation, 7740 Milestone Parkway, Suite 400, Hanover, MD 21076

14. ABSTRACT

The Low-Band Radio Frequency (RF) Intelligent Distribution Resource (LowRIDR) concept divides the architecture into the front-end RF resources and the back-end digital resources responsible for digital conditioning and distribution. The Distribution and Conditioning Subsystem (DCS) is responsible for performing this latter functionality. This report documents the Phase 1 development efforts of the DCS, demonstrating the basic functionality using commercially available Software Defined Radios (SDR) from Ettus.

15. SUBJECT TERMS

16. SECURITY CLASSIFICATION OF:			17. LIMITATION OF ABSTRACT	18. NUMBER OF PAGES	19a. NAME OF RESPONSIBLE PERSON
a. REPORT	**b. ABSTRACT**	**c. THIS PAGE**			W. Mark Dorsey
Unclassified Unlimited	Unclassified Unlimited	Unclassified Unlimited	Unclassified Unlimited	37	**19b. TELEPHONE NUMBER** *(include area code)* (202) 404-5639

Standard Form 298 (Rev. 8-98)
Prescribed by ANSI Std. Z39.18

This page intentionally left blank.

CONTENTS

This page intentionally left blank.

TUTORIAL: APPLYING PHASE-MODE THEORY TO THE DESIGN OF CYL. ARRAYS

1. Introduction

The design and analysis of a large phased array is a difficult problem often handled using approximations. Finite array analysis of a large array using typical computational electromagnetic (CEM) tools is often limited by computational resources, and using measurements to do so is limited by the cost and time required to construct and characterize such an array. There are many tools available for modern phased array design that rely on approximation to make the problem tractable, many of which involve using commercially available simulation tools. A common simulation technique uses the infinite array approach, which takes advantage of the inherent symmetry in a phased array. This typically reduces the computational domain to a single element with appropriate boundary conditions that simulate an infinite periodic extension along the lattice of the array. This approach is limited in its usefulness for planar/linear arrays, with the usefulness increasing with the size of the array. This technique treats all elements as identical, and thus neglects the impact of edge effects, providing a good approximation of the impedance match and embedded element pattern only for elements *far enough* away from the edge of the array [1, 2]. In 1968, Wheeler presented a design approach for linear/planar arrays to improve the accuracy of the approximated results that combines three techniques—small array analysis, infinite array simulations, and application of a grating lobes series—and argued that none were sufficient in isolation [3]. Oliner discussed a similar approach in [4], where he discusses *element-by-element* and *periodic-structure* approaches, and Amitay suggests the inclusion of semi-infinite array simulations to isolate edge effects [5].

In this report, we outline a simulation, design, and optimization technique for cylindrical phased arrays that builds on the same techniques used in planar/linear array design. The basic simulation and analysis technique follows Fulton's work detailed in [6], and it has been implemented in a Matlab-based framework that uses ANSYS HFSS as the solver. The discussion begins with an explanation of phase-mode theory, which is the basis of our design approach where we apply phase mode-theory concepts to a wedge-shaped unit cell with boundary conditions that create infinite array conditions both circumferentially and vertically. Then, this approach is applied to the example design of a 2.0 – 10.0 GHz cylindrical phased array antenna.

2. Circular Array Overview and Terminology

A circular array consists of N antenna elements having phase centers arranged around a circle of radius R with an angular spacing of $2\pi/N$ between adjacent elements, with the z-axis being the axis of rotation. The N elements in the array are located in the x-y plane at spherical coordinates $(R, \pi/2, 2\pi n/N)$ for $n = 0, 1, \ldots, N-1$. We can also define $\xi = R\phi$ to define the circumferential distance about the aperture of the array. Far-field coordinates are defined generically as (r, θ, ϕ). The x-y plane of this configuration is shown in Fig. 1.

Manuscript approved August 29, 2019.

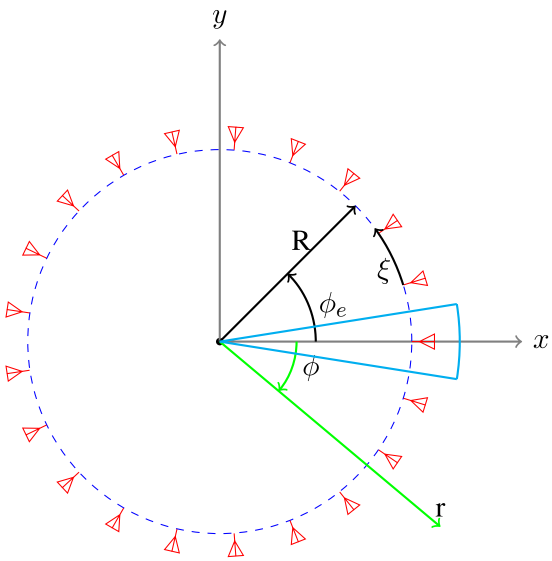

Fig. 1: An N-element circular array of radius R. This diagram shows the array elements and far-field vector. The unit cell boundaries are also shown.

The rotational symmetry of a uniform circular array (UCA) simplifies the application of infinite array simulations. This becomes apparent if we apply the concept of eigenexcitations, described in detail in [7], which are array excitation vectors that are eigenvectors of the array scattering matrix. The scattering matrix for an N-port network is an $N \times N$ matrix $\mathbf{S}$ that relates the reflected waves ($\mathbf{b}$) to the incident waves ($\mathbf{a}$) according to $\mathbf{b} = \mathbf{S}\mathbf{a}$. The scattering matrix is also related to the admittance matrix of the N-port network through $\mathbf{S} = (Y_g\mathbf{I} - \mathbf{Y})(Y_g\mathbf{I} + \mathbf{Y})^{-1}$, where $\mathbf{I}$ is the identity matrix and Y_g is the characteristic impedance of the transmission line. The admittance matrix $\mathbf{Y}$ has eigenvectors $\mathbf{e}(i)$ and corresponding eigenvalues $Y(i)$. The scattering matrix has the same set of eigenvectors, and its eigenvalues are related to those of the admittance matrix through $\Gamma(i) = \frac{Y_g - Y(i)}{Y_g + Y(i)}$ [7]. The eigenvalues of the admittance matrix are the active admittances, while the eigenvalues for the scattering matrix are the active reflection coefficients. Another parameter of interest, the *eigenpattern* $\vec{g}(i, \mathbf{k})$, is the pattern of the full array when excited by an eigenvector. Now, any arbitrary array excitation can be represented as a weighted sum of the eigenexcitations, and the corresponding array pattern can be represented as a weighted sum of the corresponding eigenvectors [8, 9].

The scattering and admittance matrix of an N-element UCA are $N \times N$ circulant matrices [10], meaning each column is obtained from the previous through a cyclic permutation [8]. For example, the admittance matrix for an N-element UCA has the following form

$$\mathbf{Y} = \begin{bmatrix} Y_0 & Y_1 & \dots & Y_{N-1} \\ Y_{N-1} & Y_0 & \dots & Y_{N-2} \\ \vdots & \vdots & \ddots & \vdots \\ Y_1 & Y_2 & \dots & Y_0 \end{bmatrix},$$

where each row (or column) vector is shifted one element to the right (or bottom) compared to the preceding row (or column). This matrix has N normalized eigenvectors of the form

$$\mathbf{e}(m) = 1/\sqrt{N}(1, w_m, w_m^2, \ldots, w_m^{N-1})^T, \text{where } w_m = \exp(j2\pi m/N). \tag{1}$$

In a phased array, this excitation corresponds to uniform-amplitude excitation with a progressive phase shift between elements.

We simulate the performance of a single element in a circular array under eigenexcitation conditions by adopting an approach that utilizes the information from N unit-cell simulations. For eigenvector $\mathbf{e}(m)$ having phase shift of $2\pi m/N$ between elements, we can enforce the proper phase shift between periodic boundary conditions of a wedge-shaped unit cell with angular separation of $2\pi/N$ between boundaries as shown in Fig. 1. The admittance and reflection coefficient obtained from this simulation gives us the eigenvalue corresponding to the given eigenexcitation. The simulation of the unit cell will also give us the current distribution in that cell. We know that the remaining $N-1$ cells will have current distributions differing only by a known progressive phase shift. Therefore, we can recreate the current distribution on the aperture by rotating a known current distribution and applying the appropriate phase shift to those replications. And, from this current distribution, we can compute the corresponding eigenpattern. Doing this for all N eigenexcitations yields the N eigenpatterns of the array using only unit-cell simulations.

The eigenexcitation form shown in (1) reveals the progressive phase shift between UCA elements, leading to the term *phase mode* often used to define an eigenexcitation. The following section will provide an overview of phase-mode theory which is applied to the efficient design of a UCA.

3. Phase-Mode Theory

The array pattern for the N-element circular can be written generically

$$\vec{F}(\mathbf{k}) = \sum_{n=1}^{N} w_n \vec{f}_n(\mathbf{k}) \tag{2}$$

in terms of complex excitation $\{w_n\}$ and complex embedded element patterns $\{\vec{f}_n(\mathbf{k})\}$, which are functions of vector wavenumber $\mathbf{k}$, as discussed in [11]. Each element in the circular array has a unique pointing direction, and thus all embedded element patterns are unique. Since the element patterns are related through rotation rather than translation, we are unable to approximate the array pattern as the product of an average embedded element pattern and an array factor. For a circular array, the embedded pattern of each element can be related to that of element N, serving here as the prototype, via

$$\vec{f}_n(\mathbf{k}) = \mathbf{R}^n \vec{f}_0(\mathbf{R}^{-n}\mathbf{k}) \tag{3}$$

for some fixed 3×3 rotation matrix $\mathbf{R}$. To ensure uniform element distribution and that no elements are duplicated, $\mathbf{R}$ should have the property that $\mathbf{R}^M = \mathbf{I}$ if and only if M is a multiple of N.

Now, we focus attention to the $\theta = \pi$ plane for the far-field pattern as shown in Fig. 1 and define co-polarized unit-vector $\hat{u}_{co}$. Using this, we define the co-polarized embedded element pattern $f(\phi) \triangleq$

$f(\vec{\phi}) \cdot \hat{u_{co}}$ and apply (2) and (3)

$$F(\theta = \pi, \phi) \triangleq F(\phi) = \sum_{n=1}^{N} w_n f_0(\phi - n\frac{2\pi}{N}) \tag{4}$$

to define the pattern in terms of prototype pattern $f_0(\phi)$.

Instead of the familiar array-pattern representation from (4), we can use the phase mode representation of the array pattern. As is well known, the outputs of an inverse discrete Fourier transform (inverse DFT or IDFT) driven by a UCA's element outputs are termed the phase modes of the array, and those phase modes can be weighted and summed to create array patterns. As will be seen in the following section, the phase mode representation is also useful in the design of a circular array.

The math is quite simple and generally follows Taylor [12] or a modern restatement in [13]. Express the prototype embedded element pattern using the usual doubly infinite Fourier series as

$$f_0(\phi) = \sum_k a_k \, \mathrm{e}^{\mathrm{j}k\phi}.$$

For $n = 0, \ldots, N-1$, element n has pattern $f_0\big(\phi - \frac{2\pi n}{N}\big)$ or, using the Fourier series,

$$f_n(\phi) = \sum_k a_k \, \mathrm{e}^{-\mathrm{j}2\pi kn/N} \, \mathrm{e}^{\mathrm{j}k\phi}.$$

For $m = 0, \ldots, N-1$, the mth phase mode then has pattern

$$Y_m(\phi) = \frac{1}{N} \sum_{n=0}^{N-1} f_n(\phi) \, \mathrm{e}^{\mathrm{j}2\pi mn/N}$$

and the array pattern is a weighted sum of the IDFT output patterns:

$$\begin{aligned} F(\phi) &= \sum_{m=0}^{N-1} W_m Y_m(\phi) \\ &= \sum_k a_k \left(\sum_{n=0}^{N-1} \Big(\frac{1}{N} \sum_{m=0}^{N-1} W_m \, \mathrm{e}^{\mathrm{j}2\pi mn/N} \Big) \, \mathrm{e}^{-\mathrm{j}2\pi kn/N} \right) \mathrm{e}^{\mathrm{j}k\phi} \, . \end{aligned}$$

The inner parentheses contain just the IDFT of W_m, with the IDFT evaluated at n. The outer parentheses in turn contain the DFT of that IDFT, with the DFT evaluated at k. The DFT inverts the IDFT, so those outer parenthesis contain just W_k. Per that DFT expression, W_k is periodic in k with period N, but for clarity we can write it as a function of a single period of W_k values as $W_{k \bmod N}$. Therefore

$$F(\phi) = \sum_k a_k \, W_{k \bmod N} \; \mathrm{e}^{\mathrm{j}k\phi} \tag{5}$$

$$= \sum_{m=0}^{N-1} W_m \sum_\ell a_{m+\ell N} \, \mathrm{e}^{\mathrm{j}(m+\ell N)\phi} \tag{6}$$

where (5) follows from the fact that the combinations of ℓ and m summed over are precisely all possible k with $k = m + \ell N$. Ultimately (5) and (6) provide two equivalent ways to look at the pattern. In (5) we see which Fourier series terms a_k are subjected to a given IFFT output weight W_m, and in (6) we see which weight W_m scales a given Fourier-series term.

Following (5), we see that the discrete sampling of the UCA excites harmonics of the desired phase modes. These harmonics are often referred to as distortion modes [14, 15]. The UCA pattern

$$F(\phi) = F_{\text{desired}}(\phi) + F_{\text{dist}}(\phi) \tag{7}$$

where

$$F_{\text{desired}}(\phi) = \sum_{m=0}^{N-1} a_m c_m e^{jm\phi} \tag{8}$$

and where the impact of the distortion modes is contained in

$$F_{\text{dist}} = \sum_{m \notin \{0,\ldots,N-1\}} a_m c_{m \text{mod} N} e^{jm\phi}. \tag{9}$$

In (8), the desired and distortion patterns are computed as weighted summations of far-field patterns that vary as $e^{jm\phi}$ that are referred to as phase modes with order m. The distortion pattern defined in (9) results from the unwanted – but unavoidable – excited harmonics of the desired phase modes.

This discussion shows that we can compute/synthesize the array pattern from a circular array using the traditional method of a weighted summation of embedded element patterns using (2). However, we can also compute the pattern in the Fourier-series domain by performing a weighted summation of phase-modes as shown in (7). In the following section, we apply phase-mode theory to the efficient design of a UCA.

4. Circular Array Design and Analysis

This section details a simulation technique used to simplify cylindrical array computer-aided design. The technique builds on that presented by Fulton in [6] and facilitates the design and simulation of cylindrical arrays, while enabling the efficient computation of embedded element patterns and the full scattering matrix.

For this discussion, we assume that we have a cylindrical array with N_{az} elements arranged about a radius R with angular increments of $\frac{2\pi}{N_{\text{az}}}$ between elements for each of the N_{el} tiers of the cylinder. This

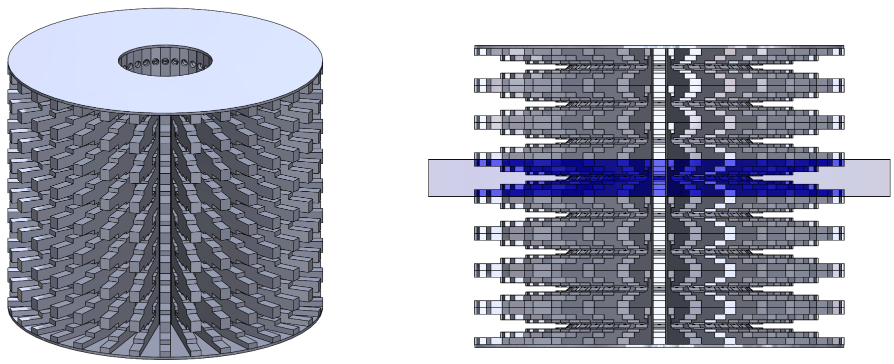

(a) Full Cylindrical Array (b) Break Down 1

Fig. 2: Simplification from cylindrical to circular array

simulation technique is centered on applying the fundamentals of phase-mode theory to a wedge-shaped unit cell representation of a cylindrical array. This simplification is important in the simulation technique, allowing us to simplify a full cylindrical array down to a unit cell with appropriate boundaries, similar to simulation techniques for planar arrays.

To begin the design process, we simplify the full cylindrical array to a unit cell. Starting out with a full cylindrical array shown in Fig. 2(a) we reduce to a circular array by pulling out a row, highlighted in Fig. 2(b). This circular cell has absorbing radiation boundaries around its circumference and master/slave boundaries on the top and bottom boundaries. The phasing between these master/slave boundaries is set to form a directional beam in the desired elevation scan angle θ_s. Note that this technique is making the assumption of a cylindrical array extended infinitely along its axis, and has the same limitations and approximations as infinite array simulations for a linear array. Moreover, this technique is easily be applied to a circular array by replacing the top and bottom master/slave boundaries with absorbing radiation boundaries.

Next, we simplify the cylindrical array further by reducing the computational domain to a single element within a wedge-shaped unit cell. Fig. 3(a) shows the circular array we pulled out in the last step, and a wedge-shaped unit cell is highlighted in Fig. 3(b). We apply a second set of master/slave boundaries on the non-parallel walls of the cell. We use these boundaries – separated by an inter-element angular spacing of $\frac{2\pi}{N}$ – to simulate the eigenexcitation (or phase-mode excitation) by applying a phase shift of $m\frac{2\pi}{N}$ between the two boundaries. This will simulate a phase-mode of index m. Iterating through indices $m = 0, 1, \ldots, N$ simulates the N unique eigenexcitations for the circular array geometry. This process must also be repeated for each unique elevation scan angle θ_s.

The key results to store from each unit-cell simulation are the unit cell radiation pattern $F^{\text{ms}}_{sim}(\theta, \phi)$ and reflection coefficient Γ^{ms}_0 for $m = 0, 1, \ldots, N$. The superscript ms in these results defines the phasing conditions of the unit cell. The m indicates the phase-mode index that defines inter-element $m\frac{2\pi}{N}$, and the s is an indicator of elevation phase progression to define scan angle θ_s. Once we have these results for each phase mode, we can follow the process of Fulton [6]. The unit-cell pattern $F^{\text{ms}}_{sim}(\theta, \phi)$ is the pattern radiated from a single-cell of the array under eigenexcitation conditions. Using the fact that all cells in the array are

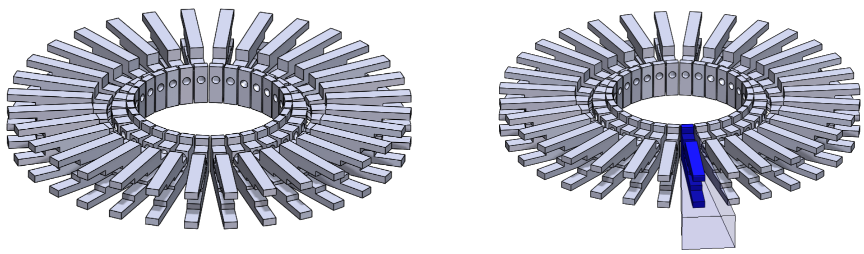

(a) Circular Array (b) Breakdown 2

Fig. 3: Simplification from circular array to wedge unit cell

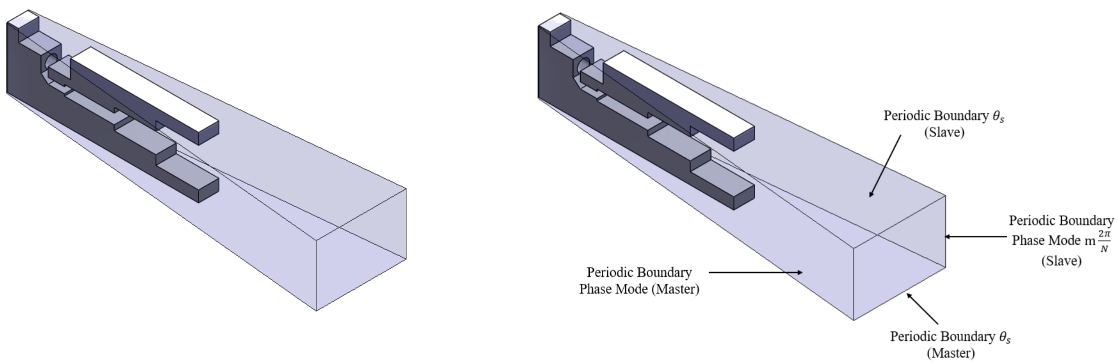

(a) Wedge Unit Cell (b) Boundaries

Fig. 4: Wedge Unit Cell

identical with the exception of a rotation, and their excitations are identical with the exception of a known phase delay, we can superimpose rotated and phase-delayed versions of $F^{\mathrm{ms}}_{sim}(\theta, \phi)$

$$F^{\mathrm{ms}}(\theta, \phi) = \sum_{n=0}^{N-1} F^{\mathrm{ms}}_{sim}(\theta, \phi - n\frac{2\pi}{N})\, \mathrm{e}^{j\,\frac{2\pi}{N}nm} \tag{10}$$

to obtain the eigenpattern (phase-mode pattern) for phase mode of order m. Now, superposition of phase modes

$$F^{s}_{emb}(\theta, \phi) = \sum_{m=0}^{N-1} F^{\mathrm{ms}}(\theta_s, \phi) \tag{11}$$

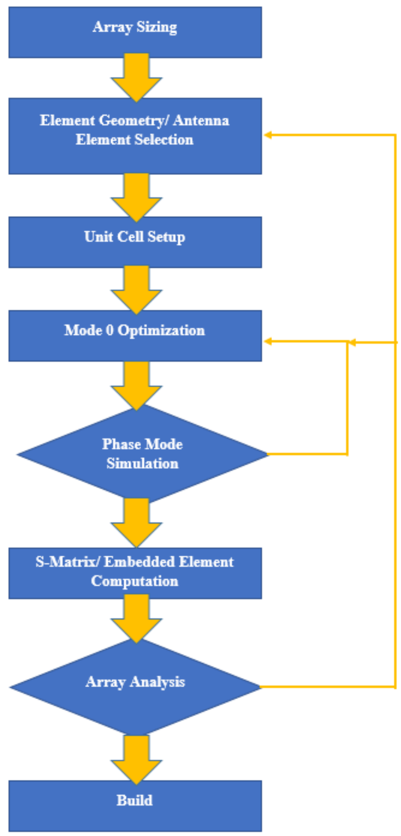

Fig. 5: Cylindrical Array Design Process

yields embedded element pattern $F^s_{emb}(\theta,\phi)$. It should be noted that the expressions in (10) and (11) are functions of elevation scan angle θ_s as they need to be solved for unique boundary conditions providing the proper phase delay between vertical master/slave boundaries.

In taking the inverse transform of the active reflection coefficient we get

$$S^s_{0n} = \frac{1}{N}\sum_{m=0}^{N-1} \Gamma_0^{\text{ms}} e^{-jnm\frac{2\pi}{N}} \tag{12}$$

a column of the scattering matrix $\mathbf{S}^s = [S^s_{\text{mn}}]$. The remaining rows of the scattering matrix, S^s_{mn}, are obtained from S^s_{0n} by noting the scattering matrix for a circular array is a circulant matrix. The superscript s carries through in the scattering matrix computation as this matrix is unique for each scan angle.

The flow chart in Fig. 5 outlines an iterative process which applies the basic simulation and processing techniques discussed in this section for designing and optimizing a cylindrical array. The procedure starts with the basics: sizing the array and selecting an appropriate element geometry. The array size is dictated either through radiation performance requirements (i.e. required gain in directional mode) or though physical constraints placed on the array itself (i.e. diameter limitations of a mast for integration). At this point, a parameterized model is developed in appropriate unit-cell boundary conditions as defined in Fig. 4(b). The element is initially optimized under mode 0 phase-mode conditions. This mode is selected because it has the widest frequency bandwidth of the phase-modes. Once mode 0 performance meets design criteria, a full phase-mode analysis is performed. The results of this are processed to compute the scattering matrix and embedded element pattern, and full array analysis is performed. This analysis most likely includes array pattern computation and active impedance calculations. If the results do not meet requirements, the process is iterated as needed until a satisfactory design is obtained and built. In the following section, we will walk through the design process of Fig. 5 step-by-step for the design of a wideband cylindrical array.

5. Design of a 2.0 – 10.0 GHz Cylindrical Array

In this section we apply the procedure of Fig. 5 to design a cylindrical array covering 2.0 – 10.0 GHz by walking through each step, explaining where key design decisions are made, showing and discussing important intermediate results and their impact on the final design.

5.1 Sizing a Cylindrical Array

A key factor in configuring a cylindrical array is determining the size: radius, height, and element count. In our analysis, we assume that the cylindrical array configuration allows it to be separated into a circular array and linear array. Sizing the vertical extent of the cylindrical array is much the same as sizing a linear array, and it is dictated by the elevation gain, beamwidth, and scanning requirements. Sizing the diameter of the cylindrical array requires a different perspective.

One method of sizing the circumference of a cylindrical array is to view an equivalent linear array as shown in Fig. 6. This equivalence follows from the phase-mode transformation [16,17]. For a given circular array size, the equivalent linear array's length is equal to the diameter of the circular array, with both arrays containing elements at $\lambda/2$ spacing. Array size is most often constrained by its given space for its application, however, sizing can also be determined by a beamwidth requirement. For a linear array beamwidth can be determined by $\phi_{3dB} = 57.3°/N$. Similarly a circular array's beamwidth can be determined by $\phi_{3dB} = 180°/M$, with N and M as the number of elements in the respective arrays [15].

Knowing a required beamwidth can help size an array due to the relationships between the frequency, radius, and beamwidth. Array beamwidth can be shown as a function of frequency and radius, seen in Fig. 7. Assuming $\lambda/2$ spacing at the high frequency, the element count for a particular array size is found by $N = \frac{2\pi R}{\lambda/2}$, dividing the circumference of the array by critical spacing at the high frequency.

For the design in this report, the diameter of the array is set to 6 inches to limit element count in the prototype array. The desired element count is set by $N = \frac{2\pi R}{\lambda/2}$, the circumference of the circular array

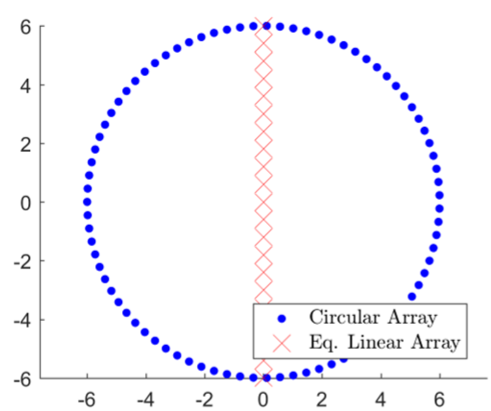

Fig. 6: Equivalent Circular - Linear Arrays

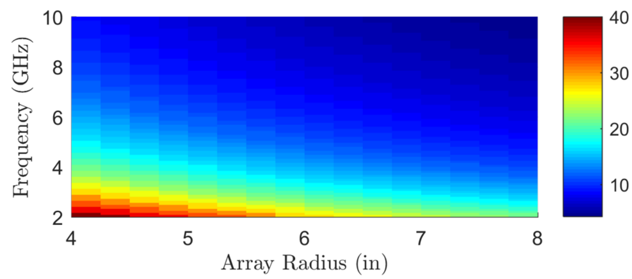

Fig. 7: Beamwidth as a Function of Frequency and Array Radius - color bar indicates beamwidth as frequency and radius vary

divided by the critical spacing at 10.0 GHz. At this size the element count is found to be $N = 32$ in azimuth. For elevation the element count is set to 8. With these dimensions, the anticipated directional-mode array patterns are shown in Fig. 8. Here we see that the cylindrical array has slightly narrower beamwidth and higher sidelobes compared to a linear array of length equal to its diameter. This results from the fact that, for a directional pattern in any given direction, the cylindrical array has a higher concentration of elements at its edges [15].

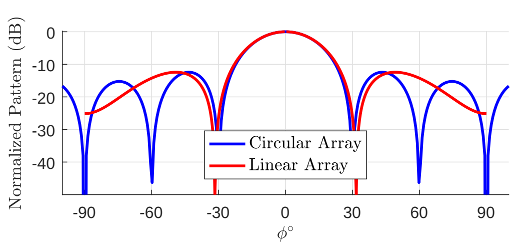

(a) 2.0 GHz

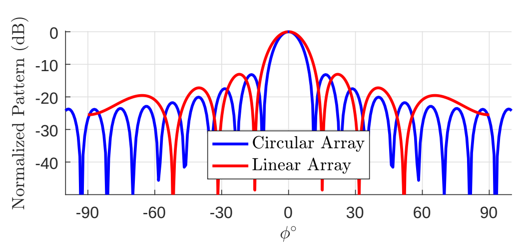

(b) 4.0 GHz

Fig. 8: Anticipated directional-mode patterns (azimuth cut) for a 6.0 inch diameter cylindrical array with 32 elements at 4.0 and 10.0 GHz. The patterns here are compared to those of a linear array with length equal to array diameter with half-wavelength element spacing at 10.0 GHz.

5.2 Element Geometry - Antenna Element Selection

Once the array sizing has been determined, a suitable antenna element must be chosen. An antenna element must be selected to enable the desired bandwidth, polarization, and manufacturing requirements. A step notch element, shown in Fig. 9, is picked for this array design. The step notch element chosen is similar to those used in [18]. This element is chosen for its wide-bandwidth capabilities, vertical polarization, and simple geometry. The simple geometry of the step notch was one of the driving factors in choosing this element.

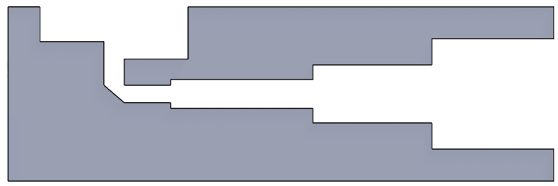

Fig. 9: Step Notch Element

5.3 Unit Cell and Boundary Condition Setup

Once the antenna element geometry is chosen, the simulation must be set up properly. As discussed in Section 3.1, the element must be placed in a wedge-shaped unit cell with appropriate boundary conditions. In Fig. 10(a) we see the step notch element contained within the wedge unit cell. Fig. 10(b) shows the setup of the master/slave periodic boundaries for the phase mode simulation. The master and slave boundaries are defined with $\frac{2\pi}{N}$ angular separation between the two walls. The slave boundary is defined such that it has a phase shift of $m\frac{2\pi}{N}$ with respect to the master boundary, where m is the phase-mode index. Then Fig. 10(c)

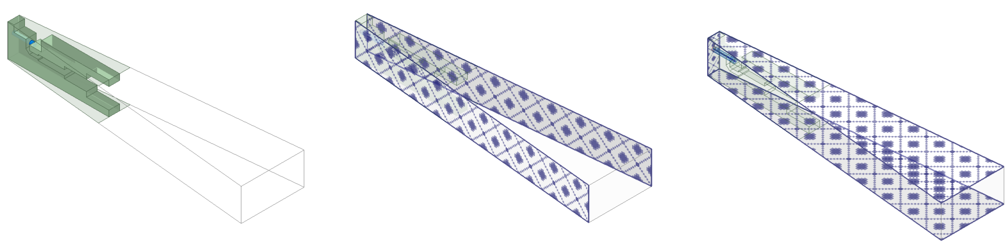

(a) Unit Cell (b) Phase Mode Boundaries (c) Elevation Boundaries

Fig. 10: HFSS Setup

depicts the master/slave boundaries for elevation scanning. The boundaries are set to apply a phase shift scanning the beam to θ_s. This phase shift is defined as $-k\Delta_z sin(\theta_s)$, where the scalar wavenumber $k = \frac{2\pi}{\lambda}$ with λ the frequency for scanning, Δ_z the spacing in elevation, and θ_s as the desired scan angle measured from the x-y plane. Once the element is fully defined in the wedge cell with the phase mode and elevation boundaries set the element is ready to be optimized.

5.4 Mode 0 Optimization

Continuing along the design process outlined in Fig. 5, the element is ready to be optimized for phase mode $m = 0$. The circumferential sampling rate of a circular array should be at least twice the highest spatial frequency [15], which tells us that our array elements should have a circumferential spacing no greater than a half-wavelength at the highest frequency. We also know that for an N-element array we can form, at most, N unique phase modes. Now, we can say that our radiating modes are bound by $-m_{\text{max}} < m \leq m_{\text{max}}$, where

$$m_{\text{max}} = \frac{N}{2} = kR = \frac{2\pi}{\lambda}R. \tag{13}$$

This relates array radius, element count, and wavelength. It also tells us that mode 0 is the mode that operates over all frequencies in the operating range of the array, which is why we focus our initial optimization stages on this mode. If elevation scanning is desired, the mode 0 optimization should include a look at a coarse sampling of desired θ_s. However, for this array we are mainly interested in performance over the horizon so the boundaries in elevation are set at broadside, with $\theta_s = 0$.

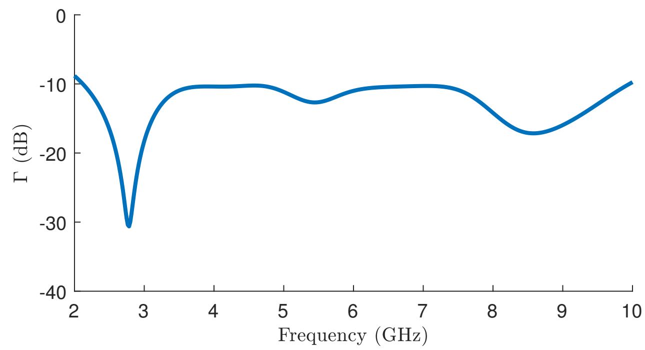

Fig. 11: Mode 0 Match

The element depicted in Fig. 10(a) is optimized over $2 - 10$ GHz for $m = 0$ and $\theta_s = 0$. The cost function minimized in the optimization

$$g_{\text{cost}} = \textbf{max}(|\Gamma(f) + 10_{\text{dB}}|)$$

pushes the active reflection coefficient $\Gamma(f)$ below the target value of -10 dB over the desired bandwidth of $2 - 10$ GHz, shown in Fig. 11, demonstrating that the element is well matched. The unit cell patterns for mode 0 are shown with Fig. 12(a) the azimuth patterns and Fig. 12(b) the elevation patterns, where azimuth is defined as the polar angle ϕ and elevation as $\theta - \pi$, the angle off of the xy plane.

The optimized element can be seen in Fig. 13 with dimensions shown in Table 1. From the single element, we can form the full column element by stacking the single element using $\lambda/2$ spacing at 10 GHz, shown in Fig. 14 with dimensions also shown in Table 1.

5.5 Phase Mode Simulation

Once the element is properly optimized the next step in the design process is to run the full simulation of phase modes and elevation scan angles. Recalling that the boundaries on the azimuthal walls are set to have

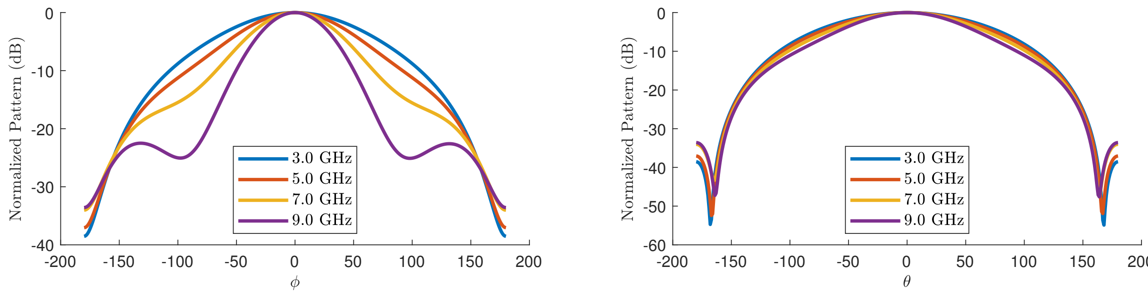

(a) Azimuth Patterns (b) Elevation Patterns

Fig. 12: Unit Cell Patterns

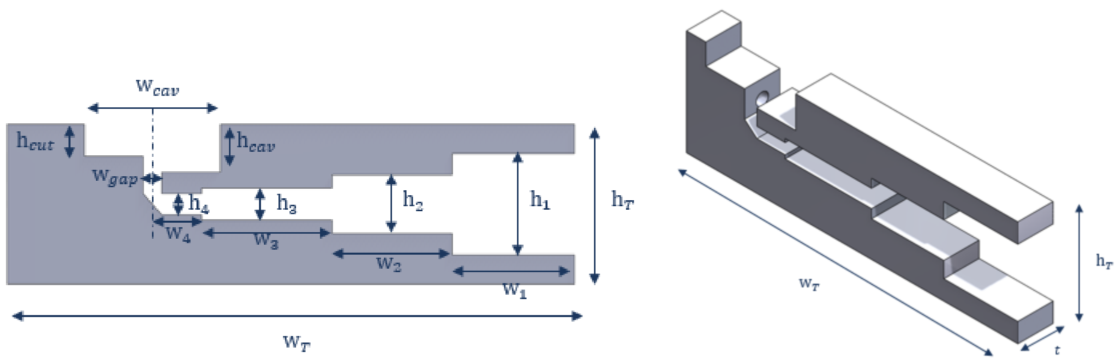

(a) Front View (b)

Fig. 13: Detailed View of Step Notch Element. Dimensions are provided in Table 1

$m\frac{2\pi}{N}$ phase shift, m is run as a parametric sweep for $m = 0, ..., N-1$ thus obtaining all the unique phase modes for the array. To obtain all desired θ_s, this process of simulating the phase modes for $m = 0, ..., N-1$ would be repeated for each scan angle. However, as mentioned before, for this array we are only concerned about broadside so the phase mode sweep is run for only $\theta_s = 0$.

One of the outputs of these parametric simulations is Γ_0^{ms}, the active reflection coefficient as a function of frequency, phase-mode index m, elevation and scan angle θ_s for element index 0. Reflection coefficients are plotted in Fig. 15 as a function of phase-mode index for various frequencies. Here, we see that more modes are well-matched at higher frequencies, which is an expected result given (13).

From the active reflection coefficient data, we can compose the contour plot of the reflection coefficient Γ for all phase modes, shown in Fig. 16. It can be seen again that mode 0 is matched from $2-10$ GHz, however, as we move to higher order modes they are only well matched at the higher frequencies. This is due

Table 1: Element Dimensions

Parameter	*Value*
h_t	0.60 in
h_1	0.38 in
h_2	0.20 in
h_3	0.10 in
h_4	0.07 in
h_{cav}	0.18 in
h_{cut}	0.12 in
w_t	1.88 in
w_1	0.42 in
w_2	0.41 in
w_3	0.49 in
w_4	0.16 in
w_{gap}	0.07 in
w_{cav}	0.51 in
t	0.20 in
h_{t_col}	4.88 in
w_{t_col}	2.13 in
e_{sp}	0.60 in

Fig. 14: Column Element

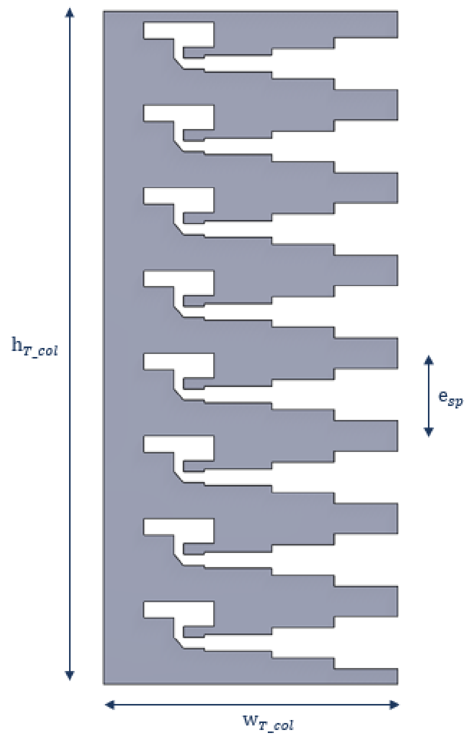

to the bounding caused by the theoretical limits of well-matched modes from (13). These limits are shown as the white lines on the contour plot, tracing the limits of $m_{max} = \pm\frac{2\pi R}{\lambda}$, and showing good agreement of the theory discussion to the simulated results.

The patterns obtained from the unit-cell simulation are not entirely useful on their own, but they are combined in post processing to create the patterns for eigenexcitations by applying (10).

5.6 S-Matrix and Embedded Element Computation

At this point all necessary information is available from the simulations in HFSS and must be exported to perform the S-matrix and embedded element pattern computations. This is where the HFSS-MATLAB script that was developed is implemented. This script exports the active reflection coefficient data as well as the unit cell patterns for azimuth and elevation cuts for all simulated phase modes (and scan angles if multiple cases were run). From here the S-Matrix can be obtained using (12), if desired, then the active reflection coefficients of the array for any arbitrary excitement are obtained.

Once the active reflection coefficient information is processed the embedded element patterns need to be computed. To do this, we take the unit cell patterns from HFSS, like Fig. 12(a) and Fig. 12(b), for all simulated phase modes and apply (11). In doing so, we end up with embedded element patterns shown in Fig. 17 for select frequencies. In order to verify that the simulation technique is valid and the patterns are correct, a full array analysis was set up and run in CST Microwave Studio to compare results. The

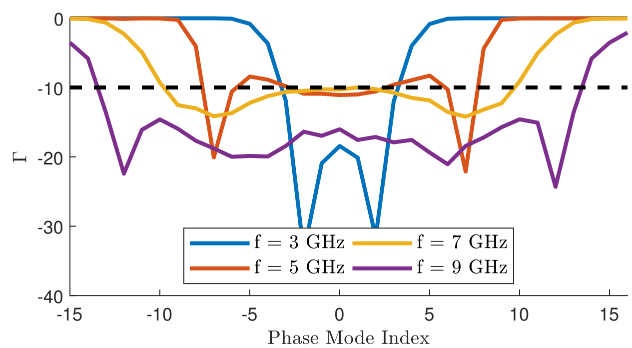

Fig. 15: Simulated reflection coefficient for the phase modes of the cylindrical array at various frequencies

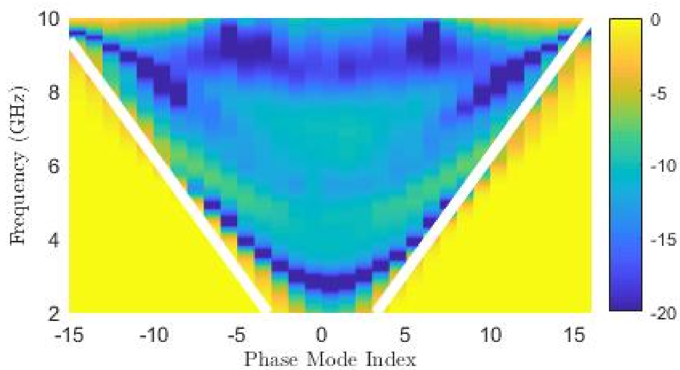

Fig. 16: Simulated reflection coefficient for the phase modes of the cylindrical array. White lines define the theoretical limits for well-matched phase modes.

pattern comparisons shown in Fig. 18, demonstrate good agreement between full array simulation and the simulation technique used, therefore validating the method.

5.7 Array Analysis

Once the embedded elements have been computed, array performance is analyzed for the desired application(s). At this stage, we must consider the final application of the array. If the patterns do not satisfy the performance needed, we must go back in the design process, whether that be in phase mode simulation, mode 0 optimization, or even element geometry redesign, and iterate until the desired performance metrics are satisfied. The example array designed in this tutorial is not aimed at a specific application. However, we will apply a few pattern synthesis techniques to suggest possible pattern analyses that could be done to highlight achievable performance. For a complete array system design and analysis, these pattern analyses would need to be coupled with a system requirements analysis and knowledge of the beamforming architecture to be able to perform an accurate analysis.

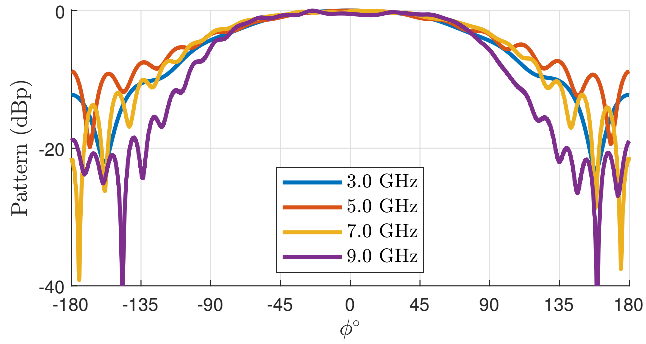

Fig. 17: Simulated Embedded Element Patterns Using Simulation Technique

5.7.1 Transmit Patterns

To maximize the power delivered to a desired receive node, we want our transmit patterns to have maximum effective radiated power (ERP). For that, we design an array excitation of the form

$$w_n = \frac{[\mathbf{f}_{\text{mb}}]_n \cdot \hat{c}}{|[\mathbf{f}_{\text{mb}}]_n \cdot \hat{c}|}, n = 0, 1, \ldots, N-1, \tag{14}$$

where $[\mathbf{f}_{\text{mb}}]_n$ is the complex pattern vector for element n in the direction of the desired mainbeam, and $\hat{c}$ is a unit-vector defining co-polarization. As discussed in [19], the downside to using a circular array for directional patterns is that each element has a unique pointing direction. Thus, for any given mainbeam direction, a majority of the elements are pointed elsewhere. Therefore, while the excitation in (14) maximizes ERP, it also will result in elevated sidelobes if all elements are used. One potential way to alleviate this issue without applying a transmit-power taper is to only excite a subset of the circular array elements. This presents a tradeoff between ERP and sidelobe level (SLL). These patterns are easily steered to any ϕ direction by simply changing the desired mainbeam direction in (14) and selecting the appropriate subset of elements.

In Fig. 19 we compare transmit patterns for the cylindrical array at 7.0 GHz using array excitations computed from (14) where $[\mathbf{f}_{\text{mb}}]_n$ is the measured embedded element pattern and $\hat{c}$ defines vertical polarization. In the first case, the transmit pattern uses all 32 elements in the array, while the second case uses only a 15-element subset. In each case, the power at each element has been limited to provide $0dB$ ERP for the phase-only case, while the second case has a total power of -3.0 dB compared to the first. This assumption was made to represent a system where the maximum power at each element is fixed. The patterns in Fig. 19 show that using all elements in the array results in a greater ERP at the expense of increased SLL.

5.7.2 Receive Patterns

On receive, the goal is typically to maximize the signal-to-noise ratio (SNR) and minimize interference from unwanted sources. In Fig. 20, we show 7.0 GHz receive patterns synthesized using the approach detailed in [20] – where second-order cone programs (SOCPs) were formulated to maximize SNR while upper

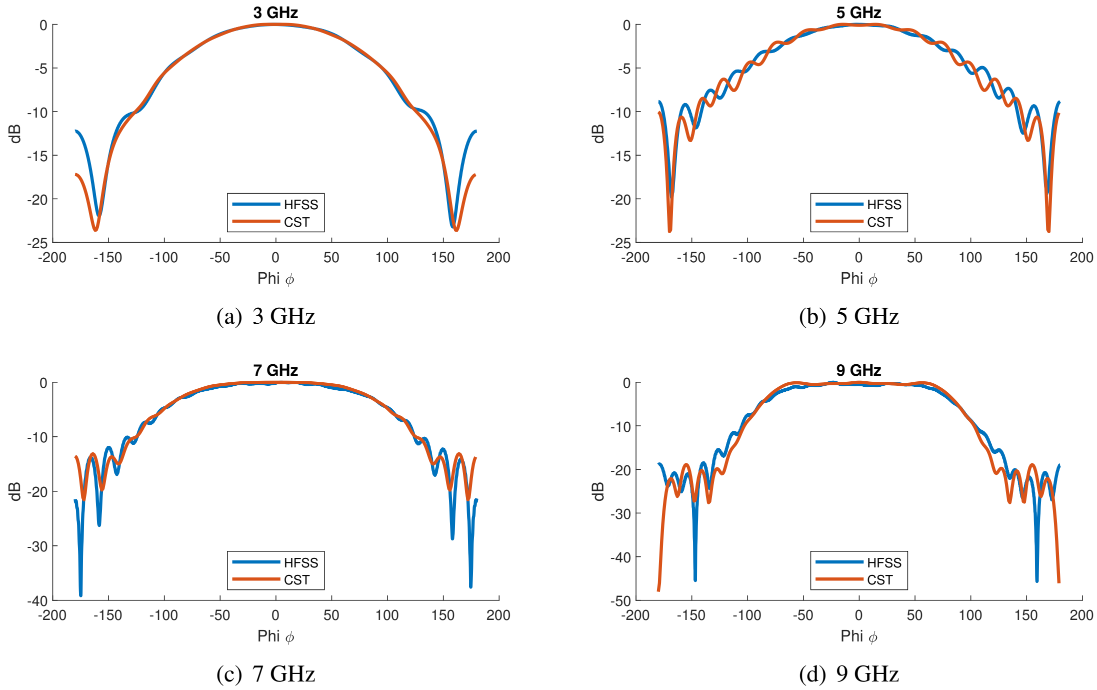

(a) 3 GHz (b) 5 GHz (c) 7 GHz (d) 9 GHz

Fig. 18: Embedded Element Pattern Verification

bounding SLL or minimize SLL while upper bounding SNR-loss. The optimal SNR pattern of Fig. 20(a) is synthesized to maximize SNR without bounds on SLL, while the curve fo 25 dB SLL upper bounds SLL at 25 dB below the peak value. The SLL-constrained pattern has a SNR-loss of 0.23 dB compared to the optimal SNR case. In Fig. 20(c), we upper bound the SNR-loss at 1.0 dB while minimizing the L_1 norm of the sidelobe region of the array pattern. This is used to minimize the total power contained in the sidelobes. The result in Fig. 20(d) instead uses the L_∞ to minimize the peak sidelobe level; this result also enforces a 1.0 dB upper bound on SNR-loss.

5.7.3 Pattern Steering

Once the array weights w_n have been designed, the resulting array pattern can then be quickly steered to any pointing direction by the technique of [13, 21]. In this section, we demonstrate the ability to steer the pattern shown in Fig. 20(a). Multiple steered patterns are shown in Fig. 21 with the mainbeam steered to $\theta_s = [45°, 90°, 180°, 300°]$. The results demonstrate that the directional beam is steered with minimal changes to SLL or beamwidth, indicating its ability to support base station applications with 360° visibility. If the array has not been designed properly (for example, if there was more phase-center variation with frequency than anticipated), then the steered patterns would exhibit greater deviation from the desired, baseline case.

When performance needs are met it is time to build the full array. The final design can be seen in Fig. 22 for the element shown earlier. The manufacturing process is discussed further in the next section.

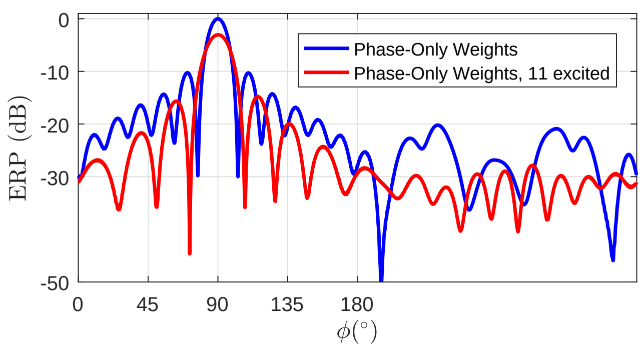

Fig. 19: Directional transmit patterns for the cylindrical array formed using phase-only excitation at 7.0 GHz.

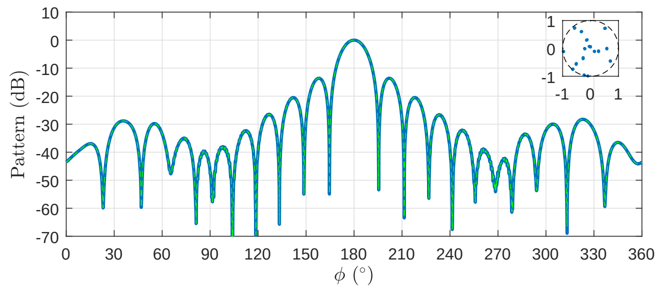

(a) Minimize taper loss

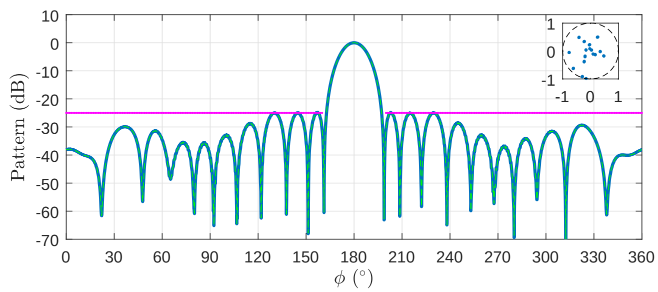

(b) Minimize taper loss with -25 dB upper bound on sidelobes

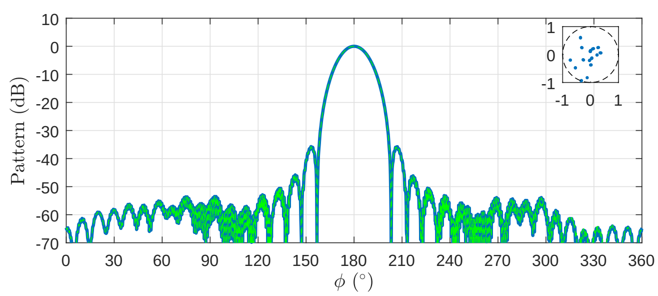

(c) L_1 minimization of sidelobes with 1.0 dB upper bound on taper loss

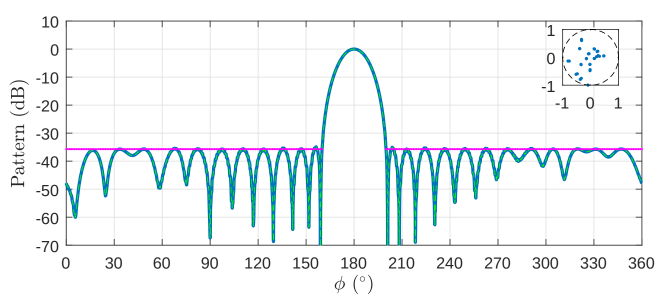

(d) L_∞ minimization of sidelobes with 1.0 dB upper bound on taper loss

Fig. 20: Optimized 7.0 GHz receive array patterns with varying on taper loss and sidelobe level.

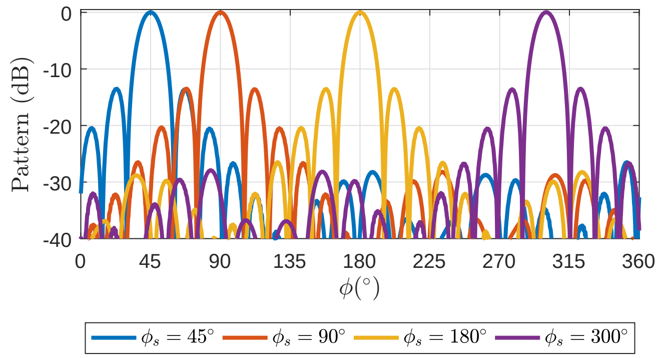

Fig. 21: Directional transmit patterns for the cylindrical array formed using phase-only excitation at 7.0 GHz.

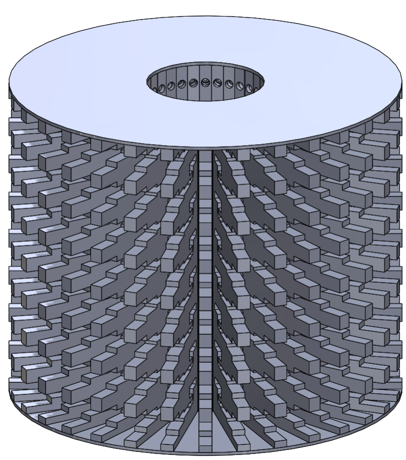

Fig. 22: Cylindrical Array Design

6. Manufactured Array and Results

This section presents the manufactured parts and apertures that were designed using the methods described in the previous section of this report. The final array design – shown in Fig. 23 – consists of 32 8-element stepped notch elements with the dimensions shown in Table 1 arranged about a 6.0 inch outer diameter. A prototype array was also designed using the design technique of this report, and it was manufactured first to validate the design technique. This array also consisted of 32 8-element columns of stepped notches, but, for this array, the elements were arranged about a 12.0 inch diameter. The larger inter-element spacing ($\lambda/2$ at 5.0 GHz instead of 10.0 GHz) alleviated the challenge of connector-integration and eased the manufacturing process to allow initial measurements to focus on design-process validation. With critical-sampling, the array would have had 64 elements and thus, it could have supported 64 unique phase modes. While this array only has 32 elements and cannot form all 64 phase modes, we were willing to sacrifice some performance for simplified manufacturing since our goal is to validate the simulation and design tools.

This prototype array is shown in Fig. 24. The plot of Fig. 25 shows that the radiating phase modes are well-matched. The mechanical and manufacturing challenges are being resolved, and an upcoming report will provide full details and characterization of the array in Fig. 23.

This report will focus on a cylindrical array that was manufactured using Electrical Discharge Machining (EDM). Other manufacturing techniques, including additive manufacturing have been applied, and those techniques are described in more in [22].

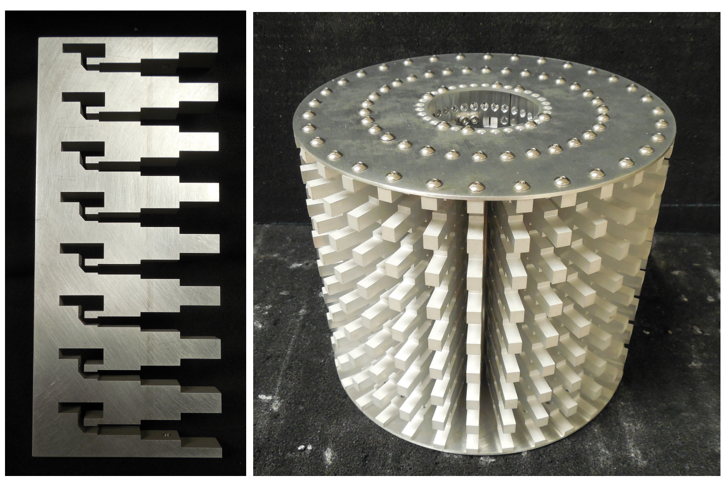

(a) 8-Element Column (b) Cylindrical Array

Fig. 23: Prototype cylindrical array. (Left) shows an 8-element column of wideband stepped-notch elements. (Right) shows a 6 inch diameter array consisting of 32 8-element columns.

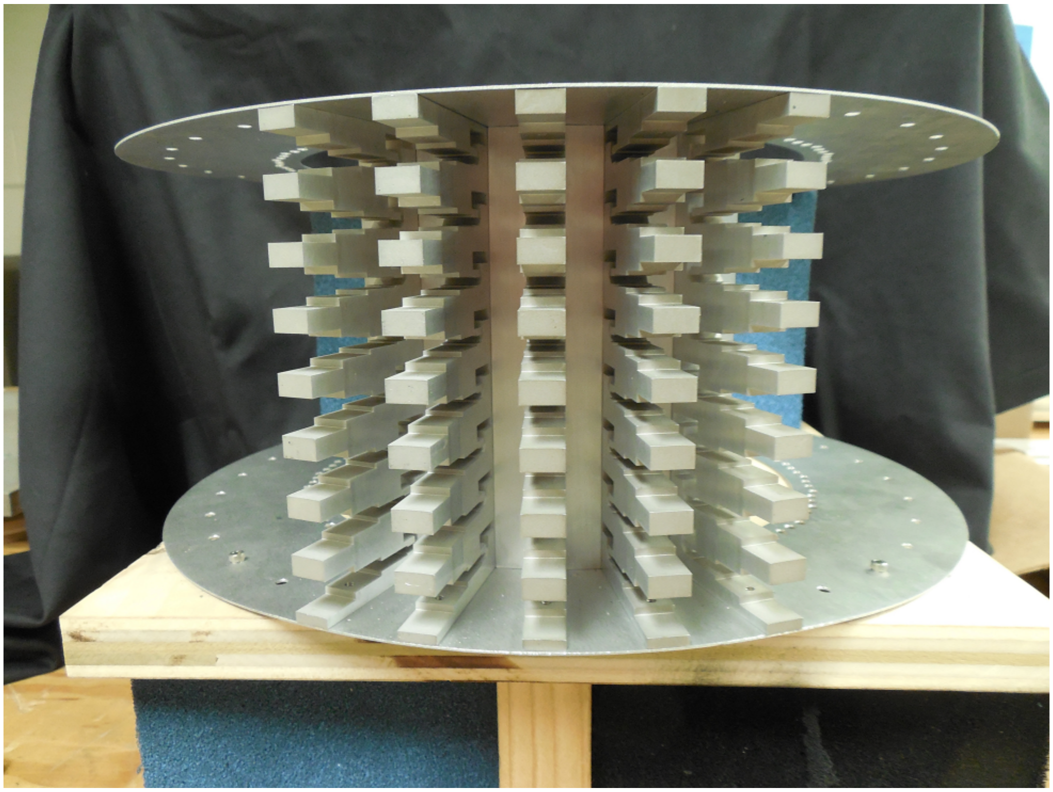

Fig. 24: Prototype cylindrical array consisting of 32 8-element columns arranged around a 12.0 inch outer diameter.

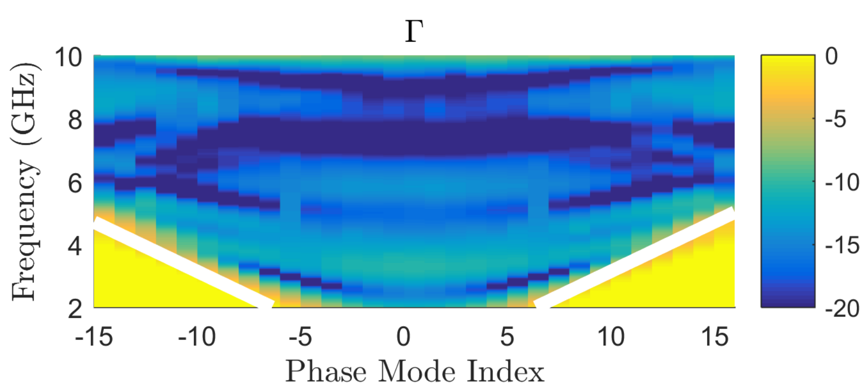

Fig. 25: Simulated reflection coefficient for the phase modes of the prototype cylindrical array shown in Fig. 24.

6.1 S-Parameter Measurements

The initial characterization of the elements in the array shown in Fig. 24 consisted of scattering parameter measurements. In these measurements, we measured the input impedance match of elements in the array with other elements terminated in a 50Ω load. The results of Fig. 26 show good agreement between measurements and simulations. Those results are for a centrally-located element, and they are indicative of the results seen at other elements in the array which indicates uniform manufacturing around the array. It should be noted that this is not the active impedance match of the element, and thus the results do not show the bandwidth that is expected. The mutual coupling between elements in the array is what leads to the wide-band performance of these elements.

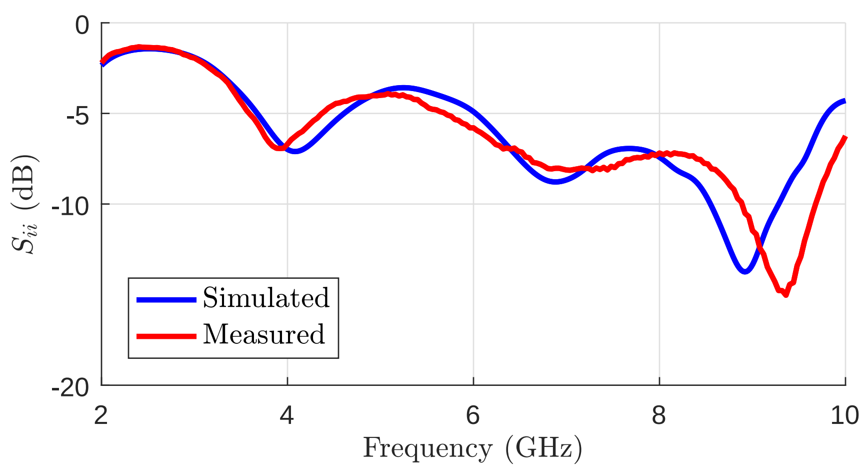

Fig. 26: Comparison between simulated and measured S_{11} for a central element of the array shown in Fig. 24.

6.2 Radiation Pattern Measurements

The focus of the cylindrical array characterization was antenna element and array pattern measurements using the planar near-field (PNF) scanner and compact range. A sampling of the measured results are shown below. Fig. 27 and Fig. 28 show PNF-measured volumetric patterns when a column of the array is excited with uniform amplitude and phase. The results are compared to simulations at 7.0 and 10.0 GHz, respectively. The measurements and simulations show good agreement in both the co- and cross-polarized components. Good agreement is also shown in Fig. 29 and Fig. 30 where we compare the patterns when three columns are excited with uniform amplitude and phase.

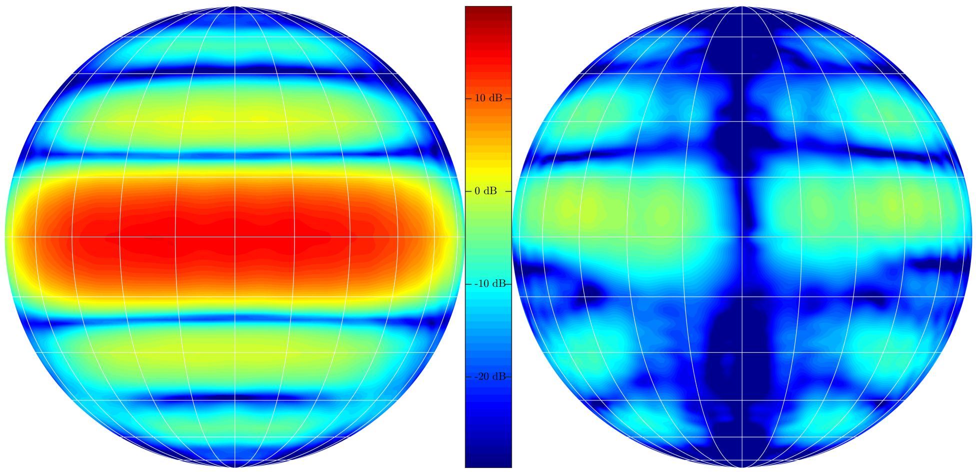

(a) Measured Pattern: 7.0 GHz

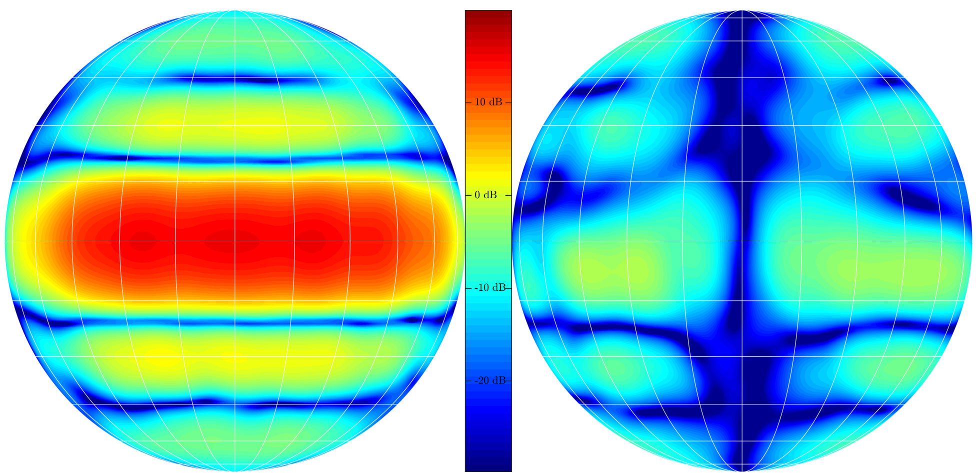

(b) Predicted Pattern: 7.0 GHz

Fig. 27: Comparison of planar near-field (PNF) measured 7.0 GHz radiation patterns to predicted (simulations) when a single 8-element column of the array from Fig. 24 is excited with uniform amplitude and phase.

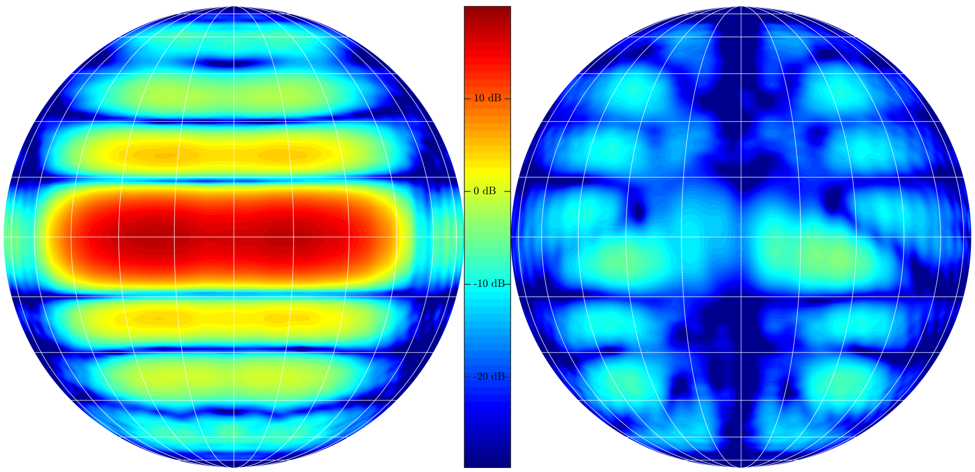

(a) Measured Pattern: 10.0 GHz

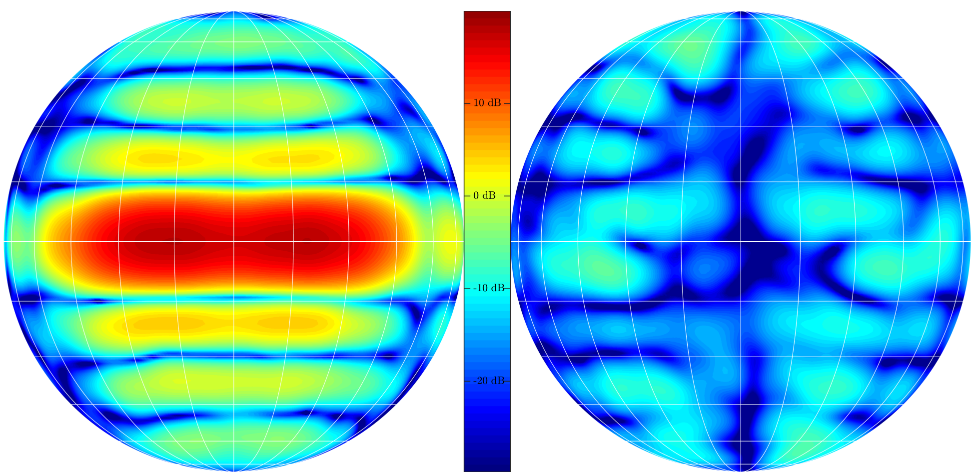

(b) Predicted Pattern: 10.0 GHz

Fig. 28: Comparison of planar near-field (PNF) measured 10.0 GHz radiation patterns to predicted (simulations) when a single 8-element column of the array from Fig. 24 is excited with uniform amplitude and phase.

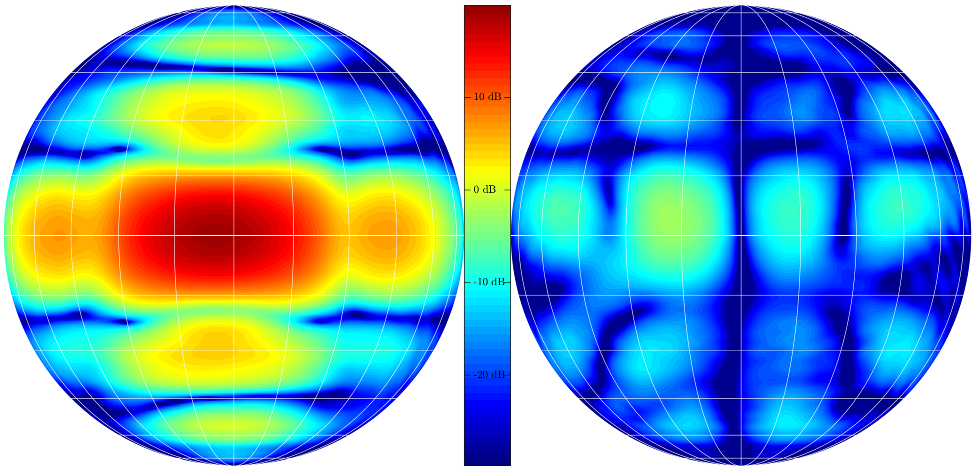

(a) Measured Pattern: 7.0 GHz

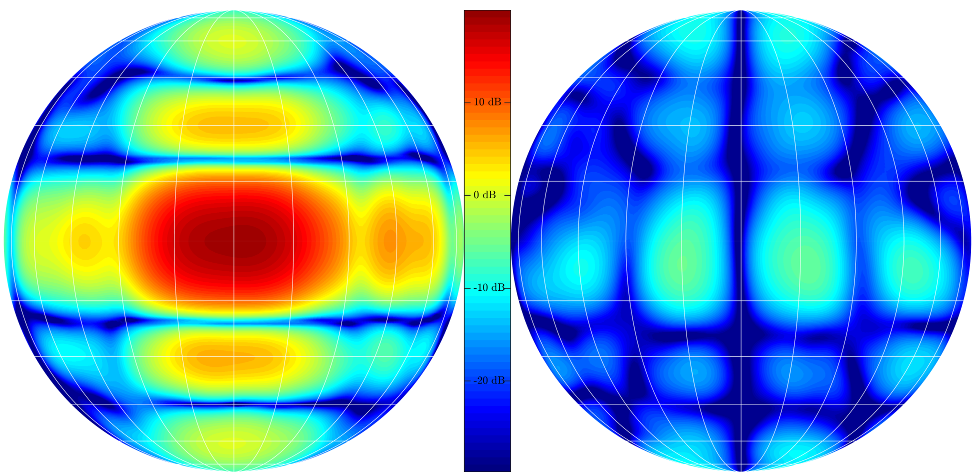

(b) Predicted Pattern: 7.0 GHz

Fig. 29: Comparison of planar near-field (PNF) measured 7.0 GHz radiation patterns to predicted (simulations) when three 8-element columns of the array from Fig. 24 are excited with uniform amplitude and phase.

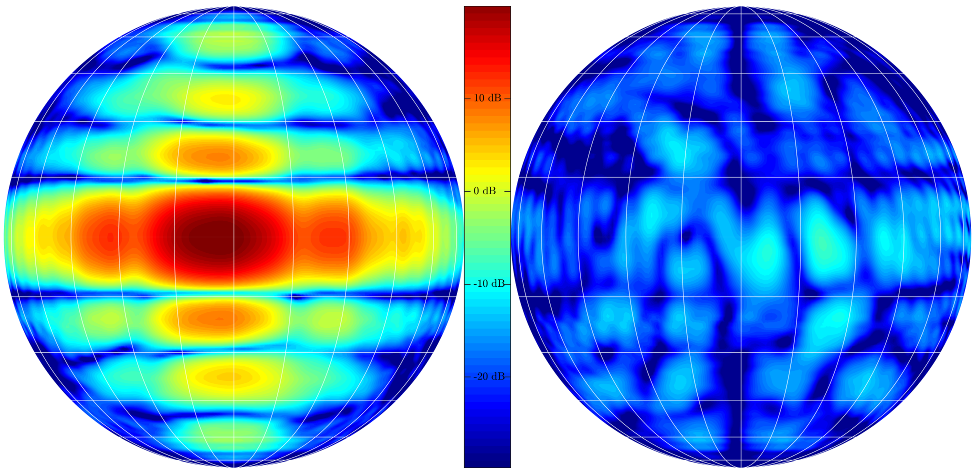

(a) Measured Pattern: 10.0 GHz

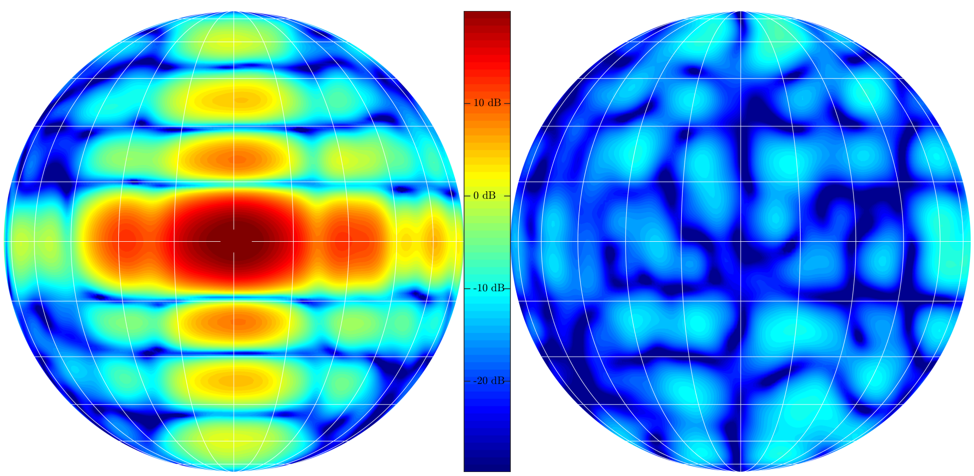

(b) Predicted Pattern: 10.0 GHz

Fig. 30: Comparison of planar near-field (PNF) measured 10.0 GHz radiation patterns to predicted (simulations) when three 8-element columns of the array from Fig. 24 are excited with uniform amplitude and phase

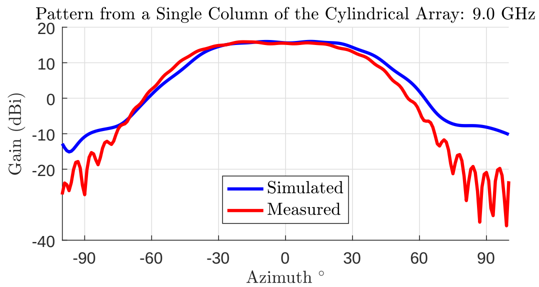

(a) Azimuth Cut

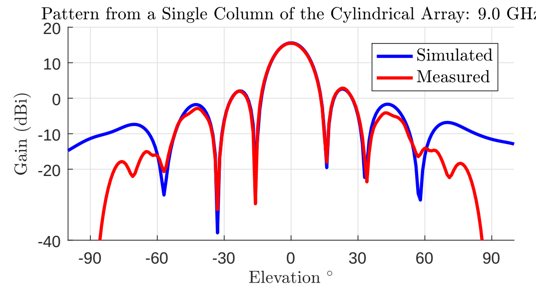

(b) Elevation Cut

Fig. 31: Comparison of azimuth and elevation patterns of a single-column of the cylindrical array. Measurement and simulations are taken at 9.0 GHz.

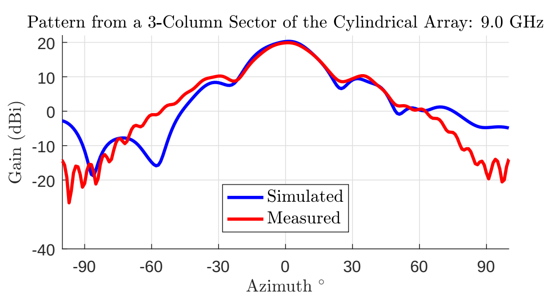

(a) Azimuth Cut

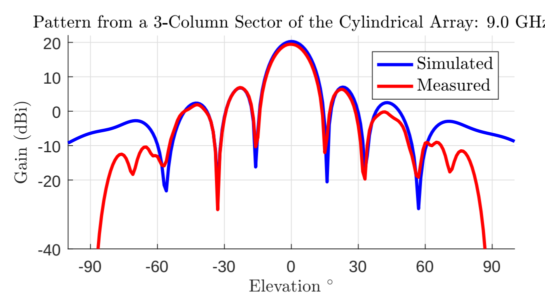

(b) Elevation Cut

Fig. 32: Comparison of azimuth and elevation patterns of a three-column sector of the cylindrical array. Measurement and simulations are taken at 9.0 GHz.

7. Conclusions

One reason cylindrical arrays are not as widely utilized as their functional benefits would suggest is the difficulty in designing them compared to the more familiar linear/planar arrays. This report develops a step-by-step approach to alleviate the design challenges of a cylindrical array, and it makes analogies to planar/linear array design where applicable to further enhance the antennas designers' understanding.

This report presents a discussion of phase-mode theory and outlines its application to the simulation, design, and optimization of circular/cylindrical phased array antennas. The basic simulation concept is an adaptation of prior work by Caleb Fulton at University of Oklahoma, and it is implemented here in a Matlab framework utilizing ANSYS HFSS as the solver.

The simulation technique discussed in this report provides a logical, step-by-step approach that streamlines the design of cylindrical arrays. This technique is then applied to the design of a wideband cylindrical array covering 2.0 – 10.0 GHz with stepped-notch elements. The array was designed, built, assembled, and characterized. The array characterization shows good agreement with simulations both in impedance match and radiation pattern measurements, thus validating the design technique presented in this report.

REFERENCES

1. H. Wheeler, "The grating-lobe series for the impedance variation in a planar phased-array antenna," *IEEE Trans. Antennas Propag.*, vol. 14, no. 6, pp. 707–714, November 1966.

2. R. Mailloux, *Phased Array Antenna Handbook*, ser. Antennas and Propagation Library. Artech House, 2005. [Online]. Available: https://books.google.com/books?id=xji1ngEACAAJ

3. H. Wheeler, "A systematic approach to the design of a radiator element for a phased-array antenna," *Proceedings of the IEEE*, vol. 56, no. 11, pp. 1940–1951, Nov 1968.

4. R. Hansen, *Microwave Scanning Antennas: Array theory and practice*, ser. Microwave Scanning Antennas. Academic Press, 1966. [Online]. Available: http://books.google.com/books?id=eyRTAAAAMAAJ

5. N. Amitay, V. Galindo, and C. Wu, *Theory and analysis of phased array antennas*. Wiley-Interscience, 1972. [Online]. Available: https://books.google.com/books?id=-xQoAQAAMAAJ

6. C. J. Fulton and A. Mirkamali, "A computer-aided technique for the analysis of embedded element patterns of cylindrical arrays [em programmer's notebook]," *IEEE Antennas and Propagation Magazine*, vol. 57, no. 3, pp. 132–138, June 2015.

7. G. V. Borgiotti and Q. Balzano, "Mutual coupling analysis of a conformal array of elements on a cylindrical surface," *IEEE Trans. Antennas Propag.*, vol. 18, no. 1, pp. 55–63, Jan 1970.

8. Q. Balzano and T. Dowling, "Mutual coupling analysis of arrays of apertures on cones," *IEEE Trans. Antennas Propag.*, vol. 22, no. 1, pp. 92–97, Jan 1974.

9. G. Borgiotti and Q. Balzano, "Analysis and element pattern design of periodic arrays of circular apertures on conducting cylinders," *IEEE Trans. Antennas Propag.*, vol. 20, no. 5, pp. 547–555, Sep 1972.

10. J. Zhou, J. Zhang, H. Wang, X. Yin, M. Tong, and J. Li, "Simple impedance matrix characterization method for uniform circular antenna arrays," in *IEEE International Symp. on Antennas and Propag.*, July 2014, pp. 943–944.

11. D. Kelley and W. Stutzman, "Array antenna pattern modeling methods that include mutual coupling effects," *IEEE Trans. Antennas Propag.*, vol. 41, no. 12, pp. 1625–1632, 1993.

12. T. Taylor, "A synthesis method for circular and cylindrical antennas composed of discrete elements," *Transactions of the IRE Professional Group on Antennas and Propagation*, vol. PGAP-3, pp. 251–261, August 1952.

13. J. O. Coleman and W. M. Dorsey, "Phase-shift steer a uniform circular array in the fourier-series domain," in *Wireless and Microwave Technology Conference (WAMICON)*, April 2017, pp. 1–4.

14. L. Josefsson and P. Persson, *Conformal Array Antenna Theory and Design*, ser. IEEE Press Series on Electromagnetic Wave Theory. Wiley, 2006. [Online]. Available: https://books.google.com/books?id=MQXZDm9IVyEC

15. A. W. Rudge, Ed., *Handbook of Antenna Design, Vol. 2*, ser. Electromagnetic Waves. Institution of Engineering and Technology, 1983. [Online]. Available: https://digital-library.theiet.org/content/books/ew/pbew015g

16. A. H. Tewfik and W. Hong, "On the equivalence of uniform circular arrays and uniform linear arrays," in *Fifth ASSP Workshop on Spectrum Estimation and Modeling*, Oct 1990, pp. 139–143.

17. M. Askari, M. Karimi, and Z. Atbaee, "Robust beamforming in circular arrays using phase-mode transformation," *IET Signal Processing*, vol. 7, no. 8, pp. 693–703, October 2013.

18. G. A. Brigham, M. Davidovitz, S. M. Duffy, and J. S. Herd, "Ultra-wideband step notch array using stripline feed," in *IEEE International Symp. on Antennas and Propag.*, June 2007, pp. 3660–3663.

19. W. M. Dorsey and D. P. Scholnik, "Transmit and receive circular array pattern synthesis for radar applications," in *IEEE Radar Conference*, May 2016, pp. 1–6.

20. W. M. Dorsey, J. O. Coleman, and W. R. Pickles, "Uniform circular array pattern synthesis using second-order cone programming," *IET Microwaves, Antennas Propagation*, vol. 9, no. 8, pp. 723–727, 2015.

21. B. Sheleg, "A matrix-fed circular array for continuous scanning," *Proceedings of the IEEE*, vol. 56, no. 11, pp. 2016–2027, Nov 1968.

22. A. Stumme, "Design of 3D printed cylindrical array with 360 degree scanning beamforming," Master's thesis, The Catholic University of America, 2019.